Supporting Information

Hierarchical Porous N/S-doped Carbon with Machine Learning to Predict Advanced Potassium-Ion Batteries

Ke Bi[a], *Yue Wang*[b,c], *and Guangyuan Zhou*[a,*]

[a] Division of Energy Materials (DNL 2201), Dalian Institute of Chemical Physics, Chinese Academy of Sciences, Dalian, 116023, China.

[b] State Key Laboratory of Rare Earth Resource Utilization, Changchun Institute of Applied Chemistry, Chinese Academy of Sciences, Changchun, 130022, China.

[c] Key Laboratory of Automobile Materials, Ministry of Education, Department of Materials Science and Engineering, Jilin University, Changchun, 130022, China.

[*] Corresponding author:

E-mail address: gyzhou@dicp.ac.cn (Guangyuan Zhou)

This supplemental file includes:

- Supplemental Figure S1 to S21
- Supplemental Table S1 to S6

The sequence is the same as they are mentioned in the main text.

1. Experimental Section

1.1. Preparation of the Precursor

The 40 g KOH and 20 g 4-nitrophenylthiourea were dissolved into 360 g water and mixed well. A cleaned lab coat was then added. After the lab coat absorbs water and infiltrates, the mixture was frozen at −10°C for 120 min. The lab coat in the mixture was completely dissolved, and the mixture was then broken into pieces after being frozen. The frozen blocks were then dried for 24 h in a lyophilizer, and the resulting product is the precursor.

1.2. Preparation of Porous Carbon

The precursor was placed in a high-temperature pipe furnace. A N_2 atmosphere was used as a protective gas. The heating rate was first increased by 5°C/min to 400°C, and then held for 120 min. It was then heated at 15°C/min to target temperatures T of 900, 1000, and 1100°C and held for 30 min. Finally, the sample was cooled naturally to room temperature. After annealing, the sample was removed and put in 1 M HCl solution. The bubbles were quickly stirred for 60 min to react. Vacuum filtering or a centrifugal method were used to separate the solid fluid. The product was then washed multiple times with ultra-pure water. The final black powder-like carbon products were named based on the annealing temperature: NS-C-900, NS-C-1000, and NS-C-1100.

1.3. Physical Characterization

The morphologies and structures were characterized by scanning electron microscopy (SEM, Zeiss Ultra 55) and transmission electron microscopy (TEM, FEI Tacnai G2 F20). The phases and compositions of the samples were characterized by X-ray diffraction (XRD, Bruker D8) with Cu Kα radiation, X-ray photoelectron spectroscopy (XPS, Thermo Scientific ESCA LAB 250 Xi) with monochromatic Al Kα radiation, and Raman spectroscopy (HORIBA LabRAM HR Evolution). The chemical functional groups were analyzed by Fourier transformation

infrared spectrometer (FTIR, NEXUS 870). The surface features and pore distributions were analyzed via nitrogen adsorption-desorption measurements on a Quantachrome Autosorb analyzer at liquid nitrogen temperature.

1.4. In Situ XRD

The in situ XRD electrode was assembled in a cell mold with a beryllium window. The NS-C-1100 electrode with an Al foil current collector was cut into a 1 × 1 cm^2 square, and the counter electrode and separator were the same as the coin cells. The specific current was 25 mA/g for the in situ XRD cell, and data were collected every 15 min.

1.5. In Situ Raman

In situ measurements were conducted through a coverslip window in an airtight chamber containing an assembled coin cell with a small hole to reveal the NS-C-1100. The potential of the cell was controlled using a single-channel Metrohm Autolab. A linear sweep rate of 0.5 mV/s was used, and Raman scans were acquired over 30 s intervals using an L50x objective, a 532 nm laser, a ~1.5-μm spot size, and ~600 mW of laser power.

1.6. In Situ TEM

The in situ discharge/charge experiments were constructed through a two-probe configuration in a Cs-corrected TEM (FEI, Titan G2). NS-C-1100 sample was milled into a nano pillar using focused ion beam (FIB, FEI Corp., Helios G4 CX). The nano pillar was welded on Cu mesh for use as the working cathode. Scratched metal K on a tungsten (W) tip was placed inside a glove box and filled with Ar gas as the reference and counter electrode. The naturally formed K_2O on the metal K served as a solid electrolyte. The nanobattery was inserted into a TEMSTM (scanning tunneling microscopy) holder (Pico Femto FE-F2) inside a glove box. The holder was then sealed in a home-made air-tight bag filled with dry Ar and transferred to the ETEM. The total time of exposure to the air was less than 2 s, which limited the extent of K_2O formation on the surface of the K metal. The nano pillar was manipulated to approach the K_2O layer, and then a potential was applied to the NS-C-1100 versus the K metal electrode to either charge or discharge the battery. Real-time visualization of the structural

and phase changes of the NS-C-1100 can be directly correlated to the electrochemical reactions based on the above configuration.

1.7. Preparation of Potassium Ion Half Cells and PIBs Pouch Cell

Electrochemical performance analyses of the potassium ion half cells used 2032-type coin cells. The powder electrodes (NS-C-900/1000/1100) were made of 80 wt.% active material, 10 wt.% Super P, and 10 wt.% CMC-Na. The slurry was coated on Cu foil to prepare the anode. These electrodes were dried in a vacuum oven at 80°C for 24 h. The mass loadings of electrode materials were 0.5–1.2 mg cm^{-2}. The assembly was performed in the glove box, potassium foil was used as the counter electrode, and a glass microfiber filter (Whatman, Grade GF/A) was used as the separator. The electrolyte was 0.8 M KPF_6 EC/DEC (1:1 by volume ratio). The PIB pouch cell was assembled in an argon-filled glove box using NS-C-1100 anode (prepared by mixing active material (80 wt.%), acetylene black (10 wt.%), and PVDF (10 wt.%) in NMP. This material was then uniformly spread onto copper foil. The mass loading of NS-C-1100 is 0.6–1.4 mg cm^{-2}. A glass fiber separator, a PB cathode (prepared by mixing active material (80 wt.%), acetylene black (10 wt.%), and PVDF (10 wt.%) in NMP were also used and uniformly spread onto aluminum foil; the mass loading of PB is 1.8–2.4 mg cm^{-2}. The electrolyte was 0.8 M KPF_6 in ethylene carbonate/dimethyl carbonate (1:1). Prior to use in the pouch cell, the NS-C-1100 anode was potassiated in a half PIB with K metal as the counter electrode. And the capacity was calculated based on the mass of anode.

1.8. Electrochemical Tests and Calculations

The galvanostatic charge-discharge process was measured using a Land battery test system. The voltage range was 0.01~3V. Cyclic voltammetry (CV) analysis was performed by employing the electrochemical workstations (CHI760E). Electrochemical impedance spectroscopy (EIS) analysis was conducted from 100 kHz to 0.1 Hz. A galvanostatic intermittent titration technique (GITT) was used to measure the apparent diffusion coefficient of K^+ in electrodes with a pulse current at 0.05 A g^{-1} for 30 min between rest intervals for 2 h. The diffusivity coefficient was estimated according to Fick's second law as follows:

$$D = \frac{4}{\pi\tau}\left(\frac{m_B V_M}{M_B S}\right)^2\left(\frac{\Delta E_s}{\Delta E_\tau}\right)^2 \quad \text{(S1)}$$

where, τ is the pulse duration, M_B is molar mass of carbon, m_B and S are the active mass and surface area for the tested electrode, V_M is the molar volume, ΔE_S and ΔE_τ can be obtained from the GITT profiles.

1.9. DFT Calculation

The Vienna ab initio simulation package (VASP) was used to perform all the density functional theory (DFT) calculations. Generalized gradient approximation (GGA) with the function of Perdew-Burke-Ernzerhof (PBE) was used to describe the electron interaction energy of exchange correlation.[1] The plane wave cutoff was set to 450 eV in all calculations. The electron energy was considered to be self-consistent when the energy change was smaller than 10^{-5} eV. The criterion for optimal convergence of geometric structure was energy change smaller than −0.01 eV. The Brillouin zones were sampled with 5 × 5 × 1 Monkhorst-Pack meshes. A vacuum layer of 20 Å was built to prevent interactions between the two repeated layers.

2. Machine Learning

2.1. Principles of Artificial Neural Network

An artificial neural network (ANN) is a nonlinear model inspired by a biological neural network. ANNs can classify and perform regression tasks according to the characteristics of external input data. ANNs have been used for various applications including to predict the dynamic viscosity of a new non-Newtonian hybrid nanofluid,[2] predict fuel cell electrocatalyst parameters,[3] predict aircraft thrust,[4] and predict meteorological drought.[5] ANN is supervised learning, which is composed of an input layer, a hidden layer, and an output layer. The hidden layer contains an indefinite number of neurons. The specific model algorithm steps are as follows:

(1) The training data is input to the input layer of the ANN, and the final output results are obtained after several hidden layers. This process is also called forward propagation.
(2) There will be errors between the output results of the forward propagation of the neural network and the target results. The loss function is constructed according to the target results and output results. MSE is generally selected as the loss function in regression problems, and Softmax is generally selected as the loss function in multi-classification problems. The loss function is propagated backward from the output layer to the input layer.
(3) During back propagation, the value of each parameter is adjusted according to the loss function. In this process, the gradient descent method is generally used to adjust the weight and bias to reduce the loss function so that the output result of forward propagation is constantly close to the target result.
(4) The training can be terminated after iterating the above three steps (training the data repeatedly) when certain constraint conditions are reached. The specific process is as follows.

The activation function in this article uses the Relu function:

$$f(x)=\begin{cases} x, & x>0 \\ 0, & x\le 0 \end{cases} \tag{S2}$$

If there are n training samples, then the mean square error of the k-th training sample on the output layer can be expressed as:

$$E_k=\frac{1}{2}\sum_{i=1}^{l}\left(\hat{y}_i^k-y_i^k\right)^2 \tag{S3}$$

where, l represents the number of neurons in the output layer; $\hat{y}_i^k$ and y_i^k are the predicted value and the true value of the i-th output neuron of the k-th sample, respectively.

The training of the neural network means that the mean square error E_k is propagated back to each hidden layer-by-layer through the chain derivation rule. Next, based on the gradient descent principle, the weight coefficient and functional neuron threshold between neurons of each layer are iteratively updated according to the following formula with the minimum mean square error of prediction error as the goal.

$$\mu^{t+1} = \mu^{t} + \Delta\mu \tag{S4}$$

where μ *r*efers to any weight value and threshold parameter.

Through multiple iterations, the output layer E_k gradually reduces the predicted value and gradually approximates the real value until the convergence conditions are met.

2.2. Model Build

Decision Tree Regressor, Gradient Boosting Regressor and other model algorithms have achieved good results in the field of battery material prediction. The algorithms in the model above are highly interpretable and can assist chemical personnel in analyzing relevant principles. However, in the case of complex structural parameters and vague mathematical descriptions, the performance of the algorithms suffer. Based on the above considerations, this paper uses the ANN model algorithm to predict potassium storage performance. The ANN model algorithm constructs a five-layer ANN network. The activation function uses Relu, the loss function uses MSE, and the optimizer uses Adam. L2 regularization is used to prevent the network from over-fitting. The programming language used in the ANN model algorithm is Python 3.7, the deep learning framework is Tensorflow 2.4.0, and the GPU is GTX 1080 Ti.

2.3. Performance Prediction of Potassium Battery Materials

First, the computer reads the structural parameters and performance database. There are 57 structural parameters (capacity performance parameters) and 71 structural parameters (ICE performance parameters). Second, the input reads the data into the model algorithm for training. The training data set is then divided into a training set and a validation set according to the 9:1 ratio. The MAE of the validation set capacity and ICE are 14.577 and 1.983, respectively. The specific measured values and predicted values of the validation set are shown in Figure 4b,c. Analysis of the validation set predicted results, and the model algorithm constructed in this paper can perform better evaluation indicators and prediction results on the validation set. Finally, three groups of capacity and ICE potassium storage properties were successfully predicted after the performance database of capacity and ICE structural parameters were predicted and input into the model algorithm. The MAE values were 8.830

and 2.390, respectively. The potassium storage performance was more accurately predicted from the perspective of the structural parameters.

2.4. Bottleneck

There are relatively few reports on the influence of d_{002}, L_a, L_c, SSA, and I_D/I_G on potassium storage performance. Although this paper has sorted out 128 capacity and ICE structural parameters performance parameters from 71 publications, the database may still have a problem due to small data volume. The ANN model algorithm constructed here can predict the potassium storage performance of this study and can provide direction and reference for future machine learning to predict the potassium storage performance. However, the applicability of this method in other potassium storage performance prediction still needs further study.

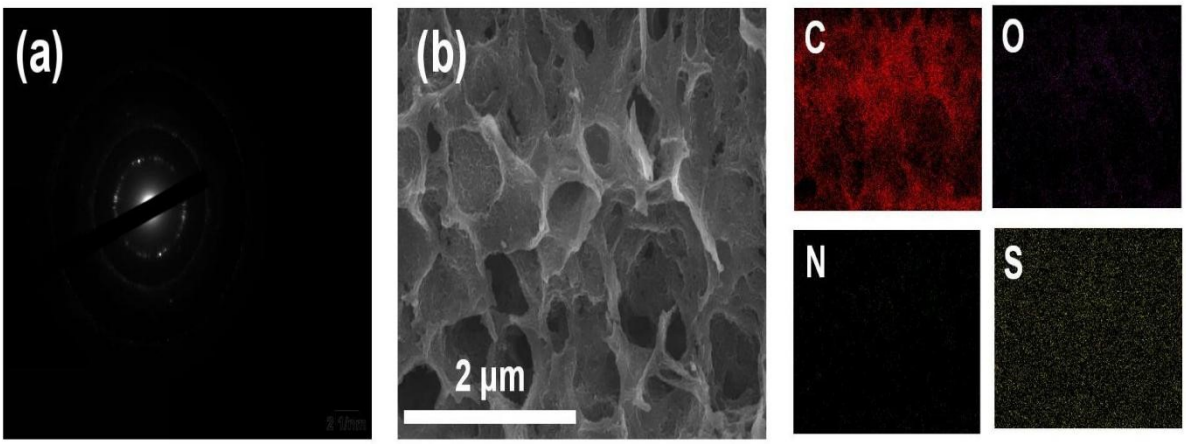

Figure S1. Physical characterization of NS-C-1100: a) SEAD pattern, b) SEM image, and corresponding elemental maps.

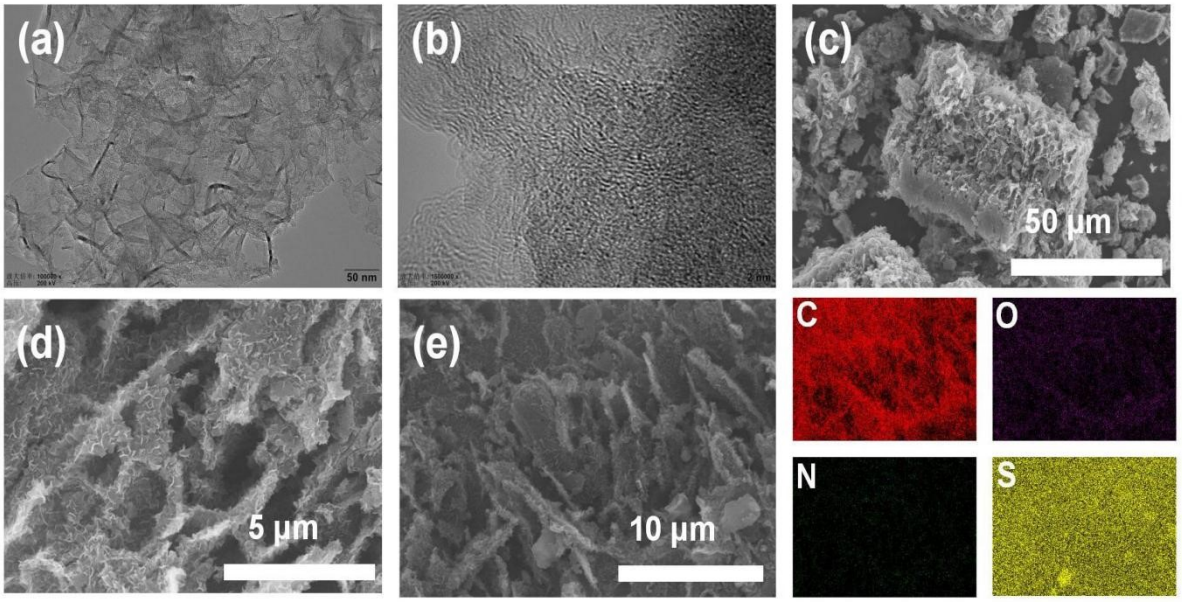

Figure S2. Physical characterization of NS-C-900: a, b) TEM images, c, d) SEM images, and e) corresponding elemental maps.

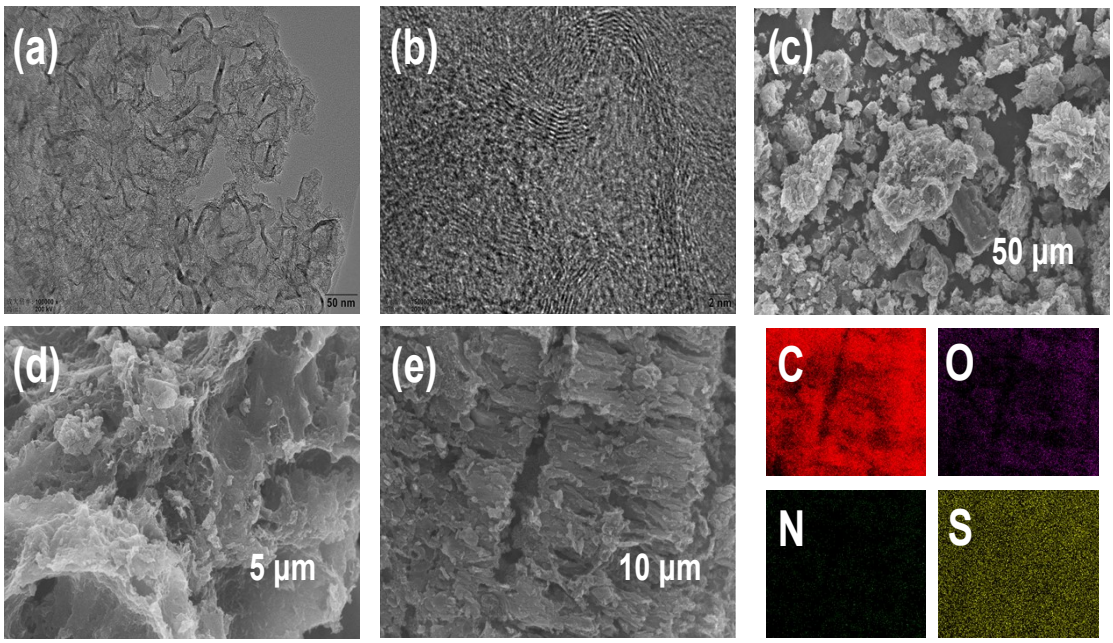

Figure S3. Physical characterization of NS-C-1000: a, b) TEM images, c, d) SEM images, and e) corresponding elemental maps.

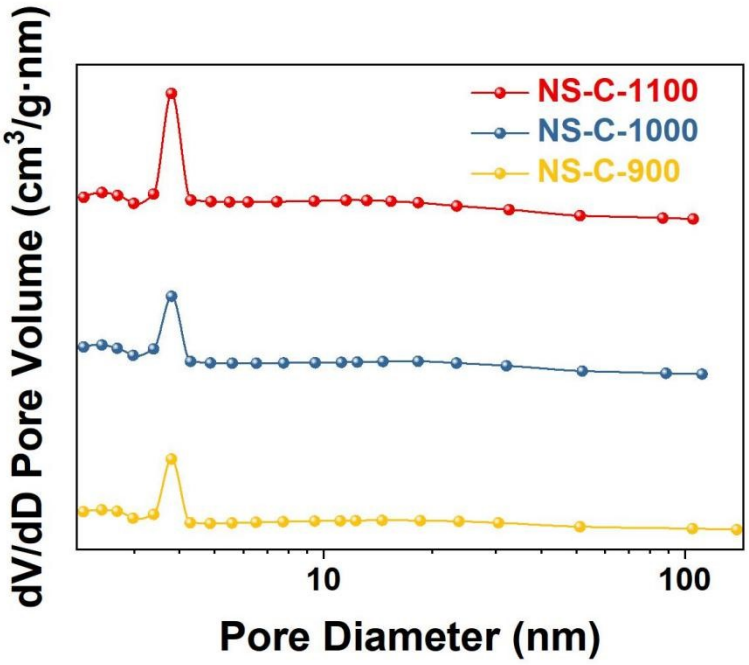

Figure S4. Pore size distribution of NS-C-900, NS-C-1000, and NS-C-1100.

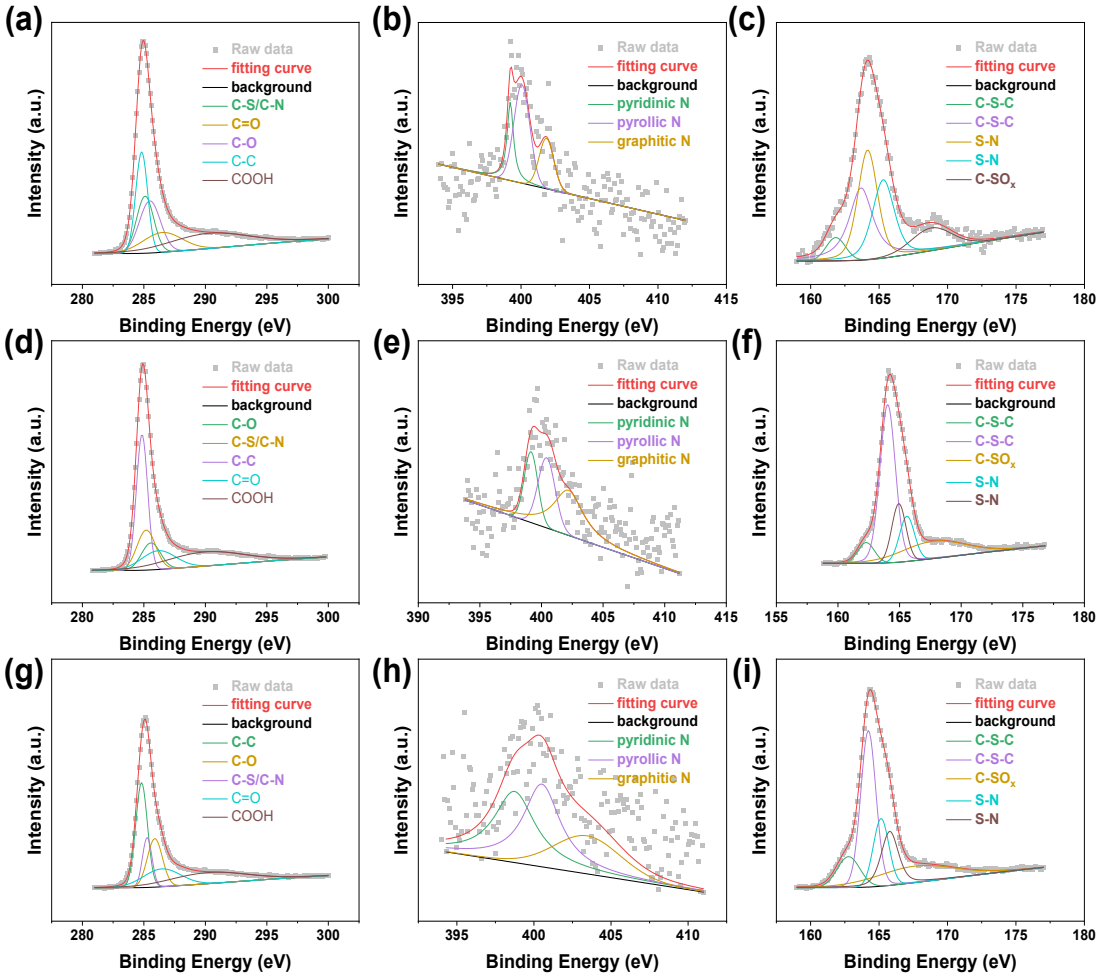

Figure S5. High resolution XPS profiles of NS-C-900, a) C1s, b) N1s, c) S2p; NS-C-1000 d) C1s, e) N1s, f) S2p; and NS-C-1100 g) C1s, h) N1s, and i) S2p.

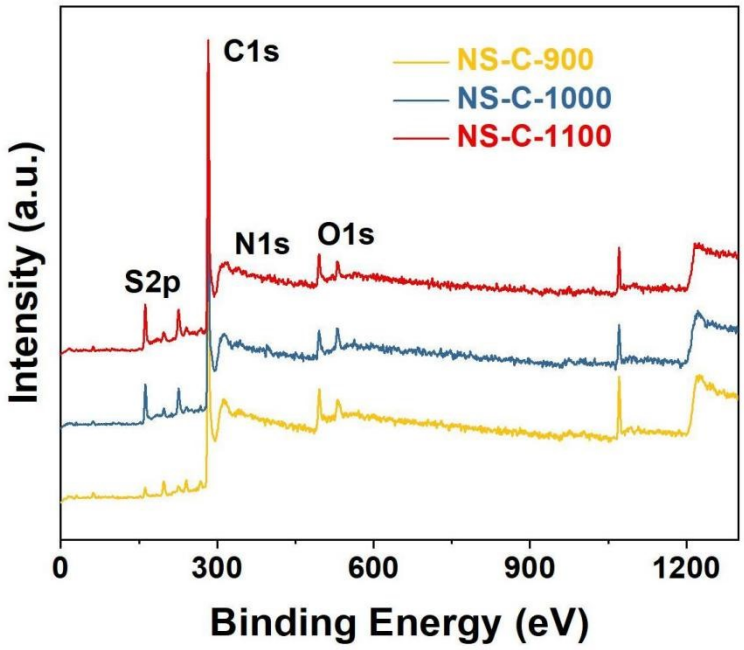

Figure S6. The XPS survey spectrum of NS-C-900, NS-C-1000, and NS-C-1100.

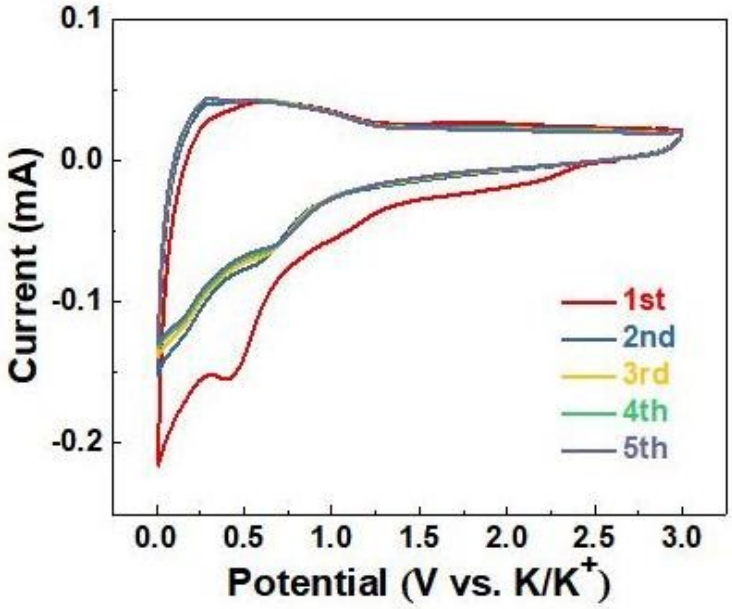

Figure S7. The first five CV curves of NS-C-900 at a scan rate of 0.2 mV/s.

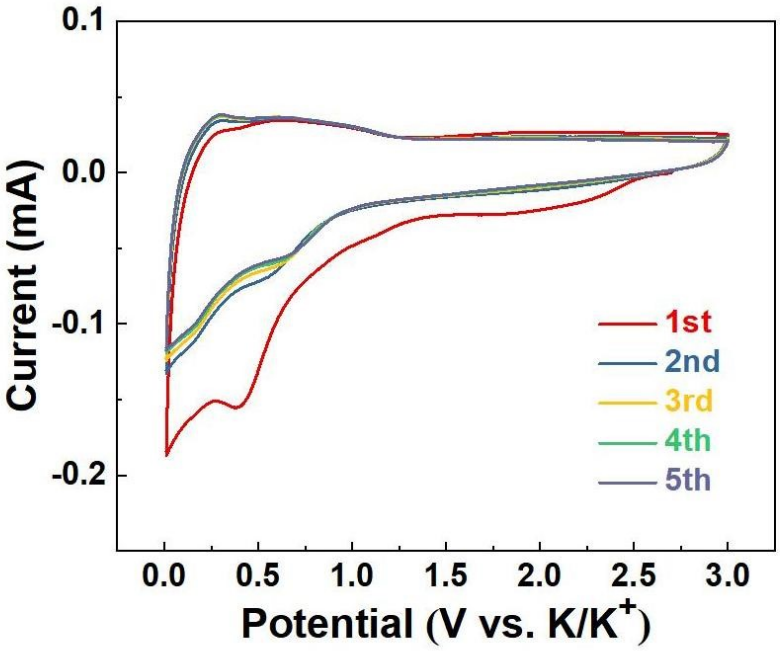

Figure S8. The first five CV curves of NS-C-1000 at a scan rate of 0.2 mV/s.

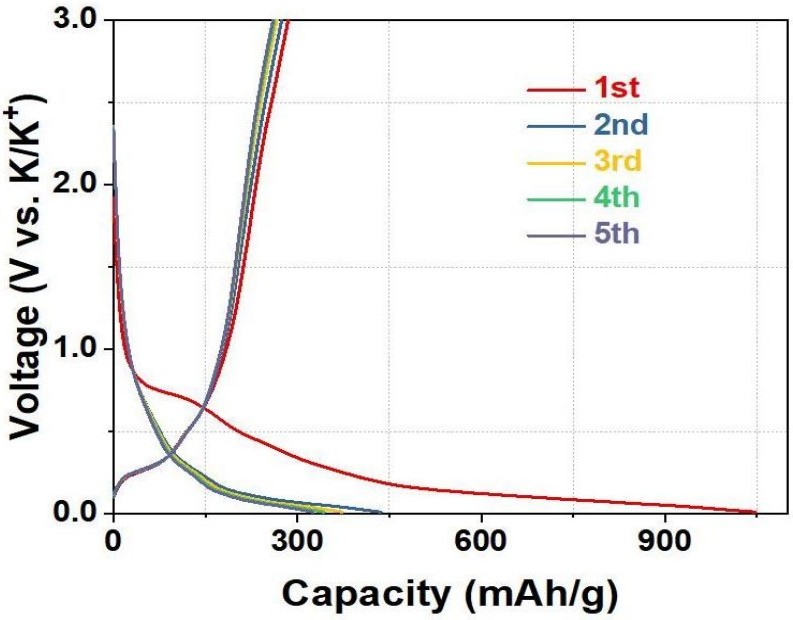

Figure S9. Galvanostatic charge/discharge voltage profiles during the first five cycles at 1 A/g for NS-C-900.

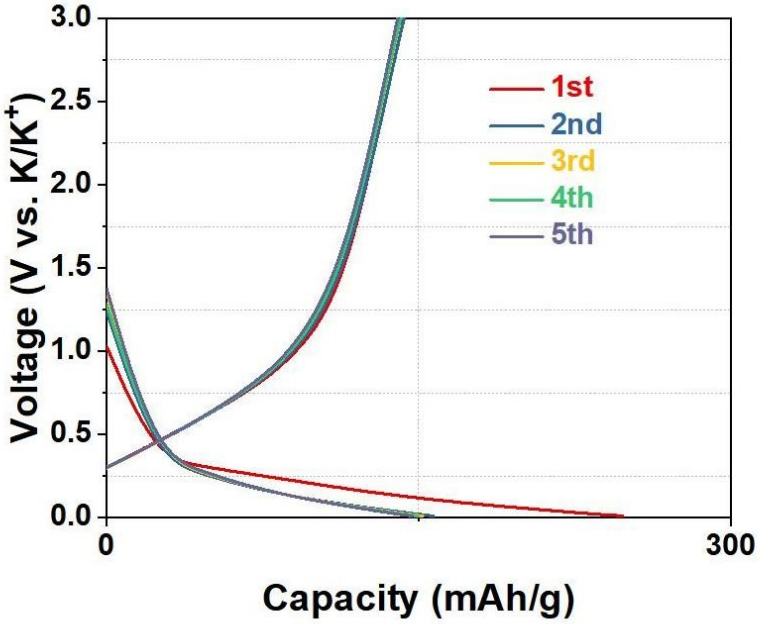

Figure S10. Galvanostatic charge/discharge voltage profiles during the first five cycles at 1 A/g for NS-C-1000.

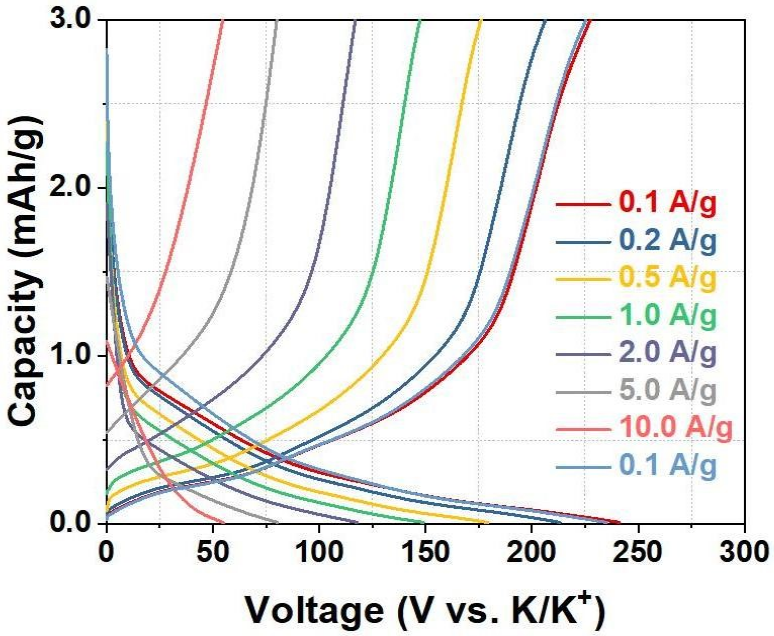

Figure S11. Galvanostatic charge/discharge voltage profiles at different current densities for NS-C-900.

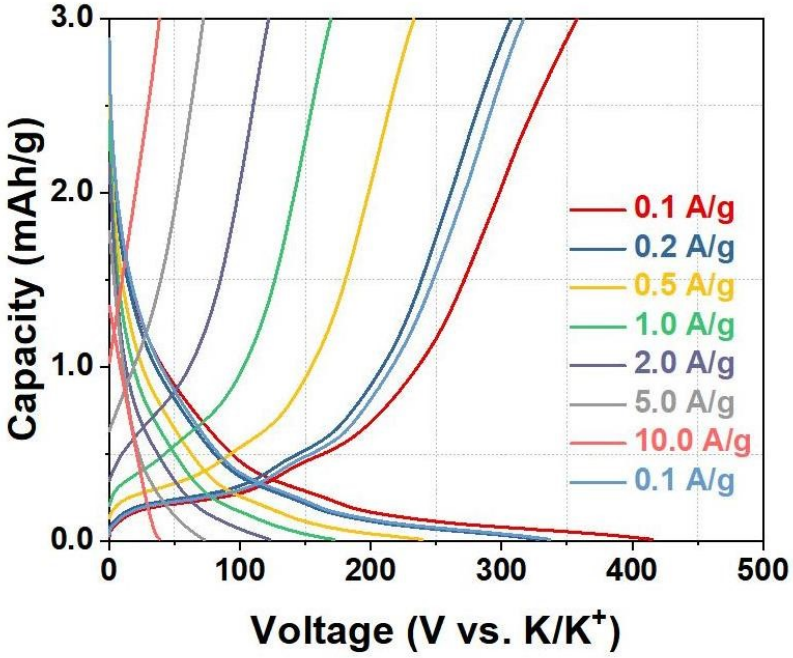

Figure S12. Galvanostatic charge/discharge voltage profiles at different current densities for NS-C-1000.

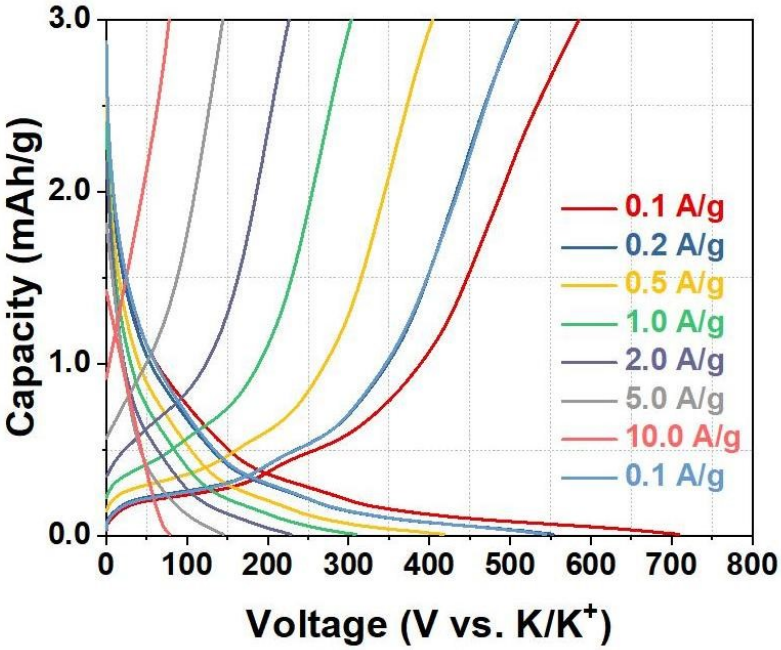

Figure S13. Galvanostatic charge/discharge voltage profiles at different current densities for NS-C-1100.

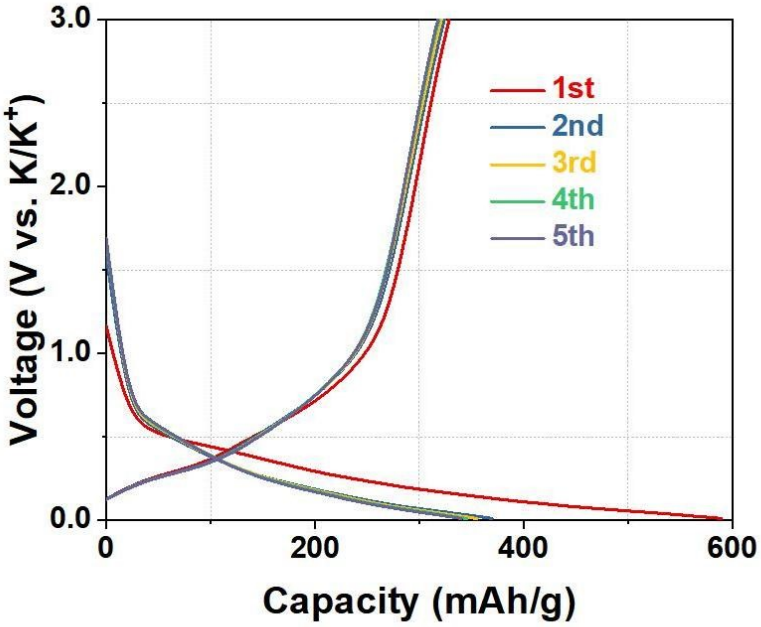

Figure S14. Galvanostatic charge/discharge voltage profiles during the first five cycles at 1 A/g for NS-C-1100 (later cycled 7000 cycles).

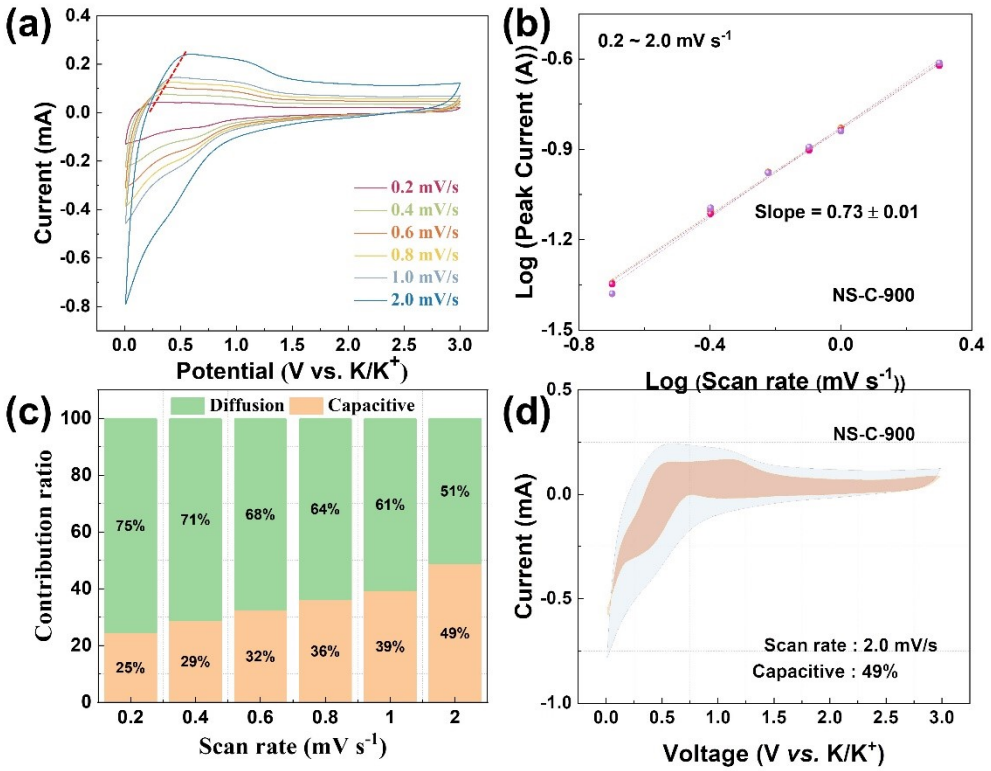

Figure S15. a) CV curves at different scan rates, b) log(*i*)–log(*v*) curve for calculating *b*, c) capacitance-controlled ratio in total capacity at different scan rates of NS-C-900, d) capacitive contribution ratio of NS-C-900 at a scan rate of 2.0 mV/s.

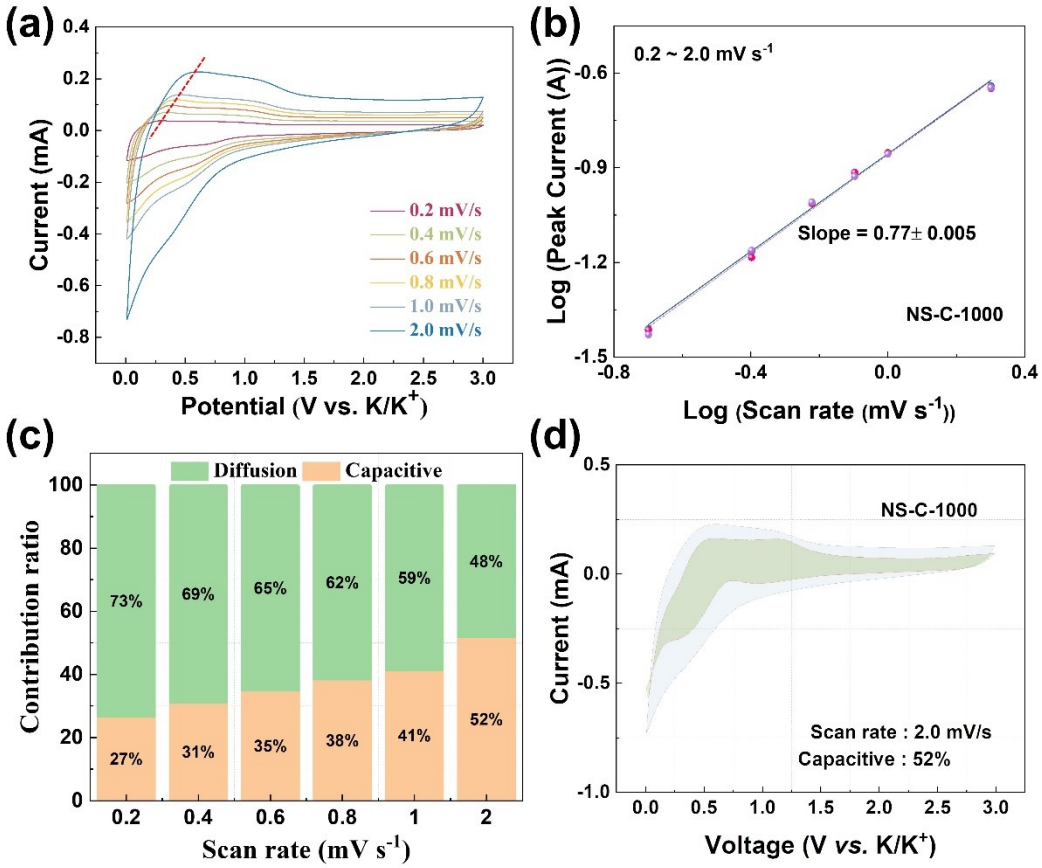

Figure S16. a) CV curves at different scan rates, b) log(*i*)–log(*v*) curve for calculating *b*, c) capacitance-controlled ratio in total capacity at different scan rates of NS-C-1000, d) capacitive contribution ratio of NS-C-1000 at a scan rate of 2.0 mV/s.

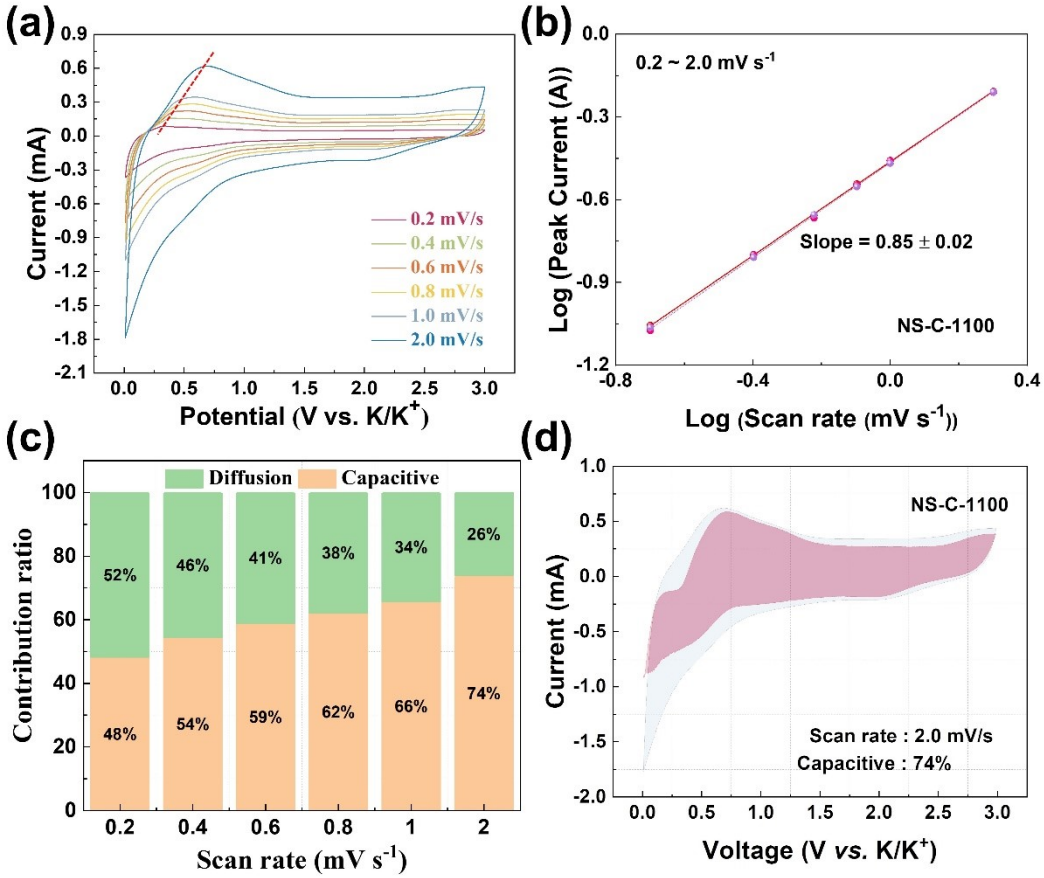

Figure S17. a) CV curves at different scan rates, b) log(*i*)–log(*v*) curve for calculating *b*, c) capacitance-controlled ratio in total capacity at different scan rates of NS-C-1100, d) capacitive contribution ratio of NS-C-1100 at a scan rate of 2.0 mV/s.

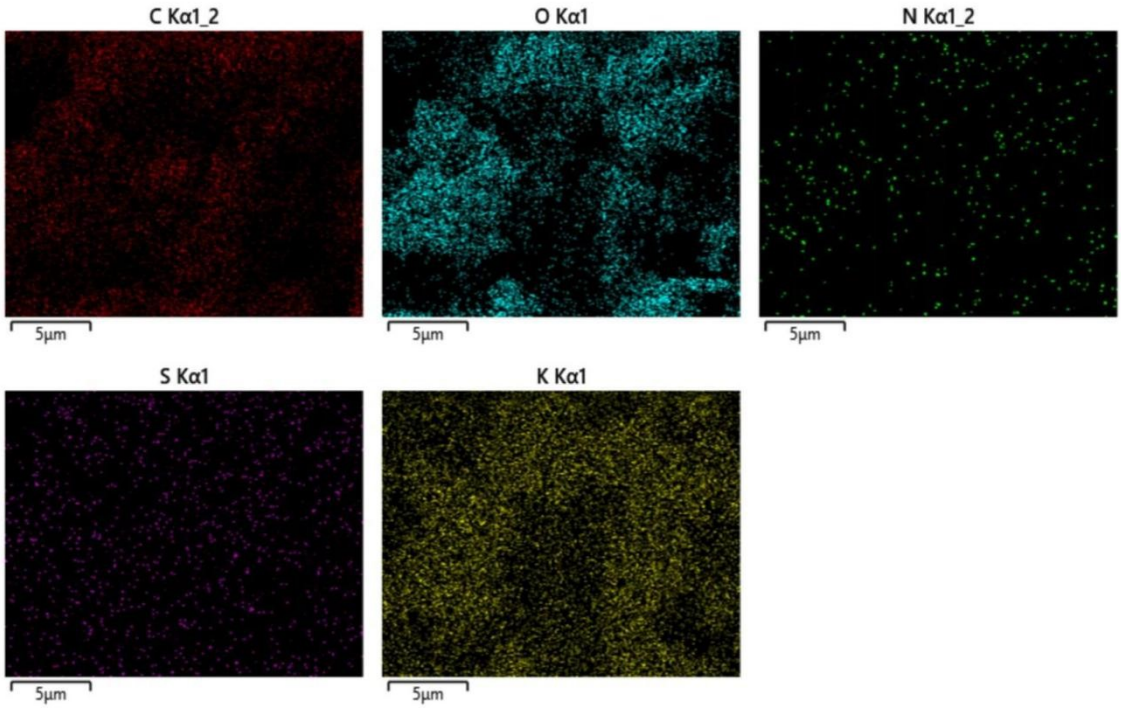

Figure S18. Elemental mapping image of C, O, N, S, and K for the first discharge to 0.01 V.

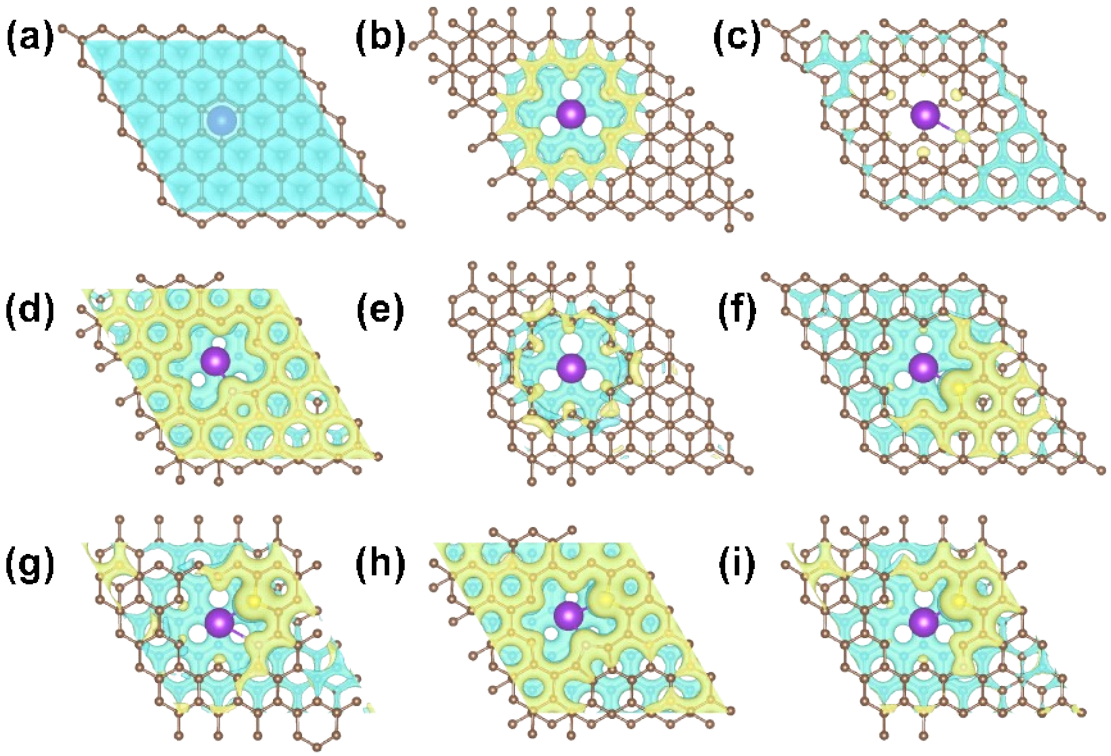

Figure S19. Top view and electron density differences of the single K adsorbed energy in the pristine, vacancy, vacancy-grN, vacancy-pdN, vacancy-plN, vacancy-S, vacancy-grNS, vacancy-pdNS, and vacancy-plNS. Yellow and blue areas represent increased and decreased electron density, respectively. The isosurfaces are the 0.015 electron bohr.[3] Brown, silver, yellow, and purple balls represent carbon, nitrogen, sulfur, and potassium atoms, respectively.

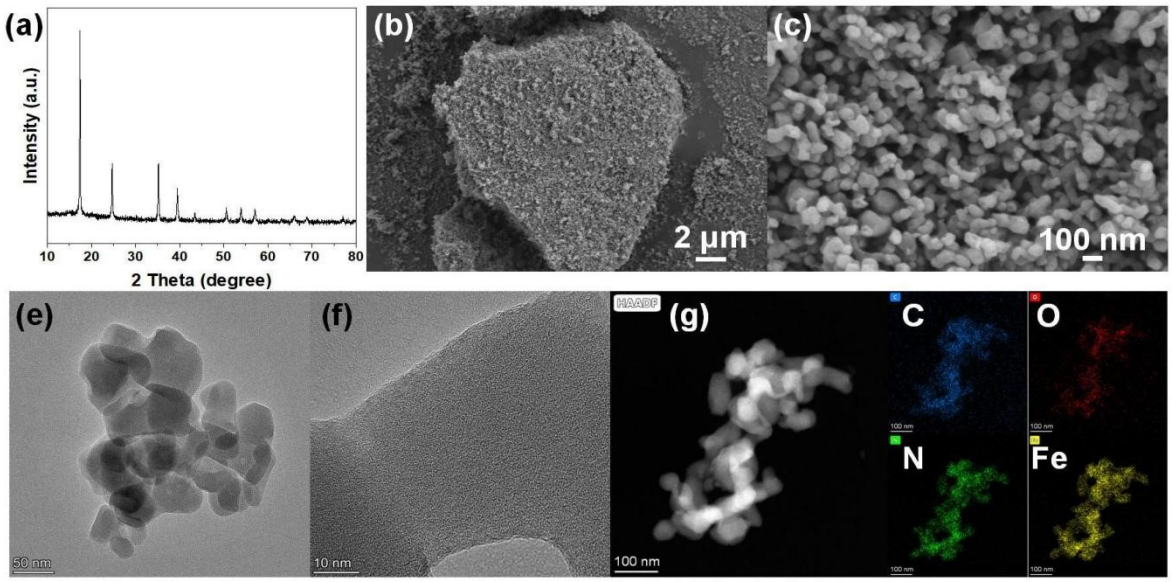

Figure S20. Physical characterizations for PB. a) XRD pattern. b, c) SEM and d, e) TEM images and corresponding elemental mappings.

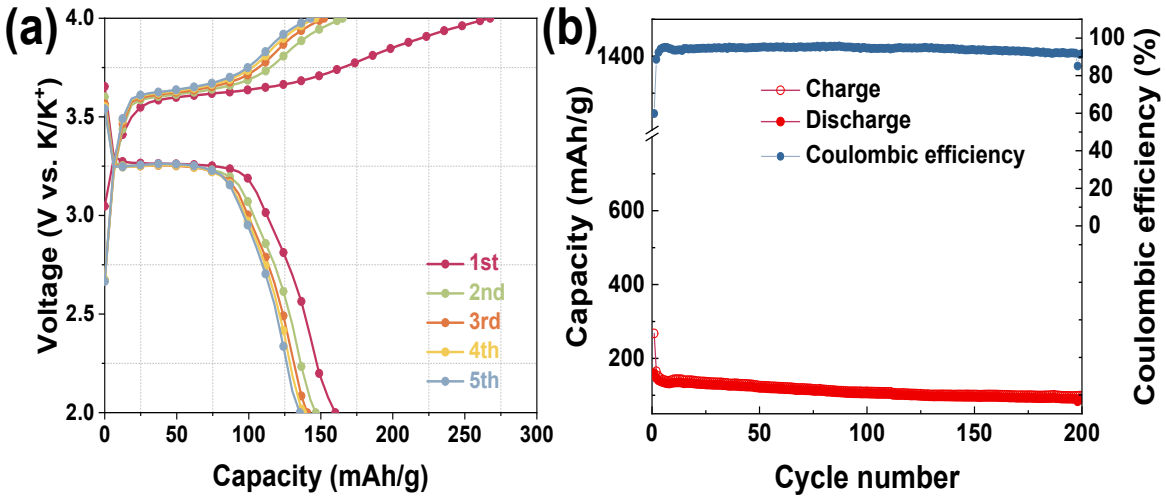

Figure S21. Electrochemical properties of PB in half-cell. a) Galvanostatic charge/discharge voltage profiles in the first five cycle at 0.1 A/g for PB. b) Cycling performance of PB at a current density of 0.1 A/g.

Table S1. Elemental contents based on XPS characterization.

	C	O	N	S
NS-C-900	**93.61**	**3.58**	**1.04**	**1.77**
NS-C-1000	**88.37**	**3.75**	**1.41**	**6.47**
NS-C-1100	**86.36**	**3.39**	**1.25**	**8.99**

Table S2. Comparison of electrochemical performances as anode of PIBs between NS-C in this work and other carbon materials.

Title	Journal	Year	1000 mA/g
Hollow N-doped carbon nanofibers provide superior potassium-storage performance	Nanoscale Adv	2020	248.4
A Flexible Multi-Channel Hollow CNT/Carbon Nanofiber Composites with S/N Co-Doping for Sodium/Potassium Ion Energy Storage	AMI	2021	200
Fast-Charging Nonaqueous Potassium-Ion Batteries Enabled by Rational Construction of Oxygen-Rich Porous Nanofiber Anodes	AMI	2021	210
Enhanced sodium and potassium ions storage of soft carbon by a S/O co-doped strategy	EA	2021	202
Understanding of the Ultrastable K-Ion Storage of Carbonaceous Anode	AFM	2018	189
Understanding mesopore volume-enhanced extra-capacity: Optimizing mesoporous carbon for high-rate and long-life potassium-storage	ESM	2020	211
Superior lithium/potassium storage capability of nitrogen-rich porous carbon nanosheets derived from petroleum coke	JMCA	2018	244
A Large Scalable and Low-Cost Sulfur/Nitrogen Dual-Doped Hard Carbon as the Negative Electrode Material for High-Performance Potassium-Ion Batteries	AEM	2019	212
Superior potassium-ion storage properties by engineering pseudocapacitive sulfur/nitrogen-containing species within three-dimensional flower-like hard carbon architectures	Carbon	2020	206
Facile and scalable synthesis of a sulfur, selenium and nitrogen co-doped hard carbon anode for high performance Na- and K-ion batteries	JMCA	2020	187.9
Sulfur-Doped Flowerlike Porous Carbon Derived from Metal-Organic Frameworks as a High-Performance Potassium-Ion Battery Anode	ACS Applied Energy Materials	2021	226.9
Fast and stable potassium-ion storage achieved by in situ molecular self-assembling N/O dual-doped carbon network	ESM	2019	205
A Site-Selective Doping Strategy of Carbon Anodes with Remarkable K-Ion Storage Capacity	Angew. Chem. Int. Ed.	2020	195
In Situ Revealing the Electroactivity of P-O and P-C Bonds in Hard Carbon for High-Capacity and Long-Life Li/K-Ion Batteries	AEM	2019	224
N/O Dual-Doped Environment-Friendly Hard Carbon as Advanced Anode for Potassium-Ion Batteries	Advanced Science	2020	254.4
Multi-forks hierarchical porous amorphous carbon with N-Doping for high-performance potassium-ion batteries	EA	2020	292.3
N/O double-doped biomass hard carbon material realizes fast and stable potassium ion storage	Carbon	2021	240.9
Soybean roots-derived N, P co-doped mesoporous hard carbon for boosting sodium and potassium-ion batteries	Carbon	2021	280
Manipulation of 2D carbon nanoplates with a core-shell structure for high-performance potassium-ion batteries	JMCA	2019	215
UIO-66-NH2-derived mesoporous carbon used as a high-performance anode for the potassium-ion battery	RSC Advances	2021	246

Carbon quantum dot micelles tailored hollow carbon anode for fast potassium and sodium storage	**Nano Energy**	**2019**	**206**
High-performance potassium ion capacitors enabled by hierarchical porous, large interlayer spacing, active site rich-nitrogen, sulfur co-doped carbon	**Carbon**	**2020**	**234.6**
Radial Pores in Nitrogen/Oxygen Dual-Doped Carbon Nanospheres Anode Boost High-Power and Ultrastable Potassium-Ion Batteries	**AFM**	**2021**	**193**
A new strategy for achieving high K^+ storage capacity with fast kinetics: realizing covalent sulfur-rich carbon by phosphorous doping	**Nanoscale**	**2021**	**299**
Phosphorus and Oxygen Dual-Doped Porous Carbon Spheres with Enhanced Reaction Kinetics as Anode Materials for High-Performance Potassium-Ion Hybrid Capacitors	**AFM**	**2021**	**258**
Toward High-Performance Capacitive Potassium-Ion Storage: A Superior Anode Material from Silicon Carbide-Derived Carbon with a Well-Developed Pore Structure	**AFM**	**2020**	**200**
Nanocomposites of reduced graphene oxide modified with mesoporous carbon layers anchored by hollow carbon spheres for energy storage	**Carbon**	**2021**	**229.1**
High potassium ion storage capacity with long cycling stability of sustainable oxygen-rich carbon nanosheets	**Nanoscale**	**2021**	**200**
Hierarchically Structured Nitrogen-Doped Carbon Microspheres for Advanced Potassium Ion Batteries	**ACS Materials Letters**	**2020**	**180**
This work			**313.5**

Table S3. Structural parameters of carbon in terms of capacity.

d_{002} (nm)	L_a (nm)	L_c (nm)	I_D/I_G	SSA_{BET} (m^2 g^{-1})	Capacity (mAh g^{-1})	Reference
0.340	34.889	10.875	0.710	126.000	240.000	6
0.351	2.610	1.350	0.770	20.330	284.000	7
0.349	3.800	1.430	0.910	26.000	271.000	7
0.348	3.930	1.880	1.030	28.500	244.000	7
0.344	5.840	3.700	1.010	52.200	436.000	8
0.336	3.690	1.210	1.050	87.500	272.000	9
0.349	7.550	2.320	0.960	3.850	255.000	10
0.335	43.871	40.816	0.340	33.400	200.000	11
0.334	145.231	74.216	0.430	6.170	209.000	12
0.330	5.799	1.602	1.180	105.000	328.000	13
0.340	5.310	2.970	0.890	68.300	255.000	14
0.339	7.738	1.554	1.060	430.000	460.000	15
0.337	5.402	23.314	1.830	1551.800	212.500	16
0.356	10.010	1.521	1.090	977.700	245.000	17
0.370	9.220	1.710	1.014	1126.000	250.000	18
0.425	8.728	2.308	1.020	1857.000	364.000	19
0.391	3.130	1.020	0.890	1030.500	265.000	20
0.353	17.599	1.551	1.670	995.000	449.000	21
0.356	43.641	4.069	1.060	69.200	301.000	22
0.370	14.547	1.710	1.000	706.740	263.000	23
0.386	2.793	2.162	0.920	1303.000	124.000	24
0.363	4.534	2.032	0.770	269.800	336.000	25
0.369	4.020	0.910	1.160	674.000	280.000	26
0.356	5.819	2.325	0.880	247.000	310.900	27
0.371	3.490	1.060	0.970	1021.100	227.000	28
0.388	3.960	0.970	1.060	983.200	212.800	29
0.386	7.737	1.707	0.920	1950.000	296.000	30
0.379	3.980	0.940	0.950	778.750	230.900	31
0.388	3.110	0.950	0.950	848.300	289.000	32
0.353	3.370	0.770	0.810	110.730	219.000	33
0.375	4.080	0.900	0.890	357.680	263.000	33
0.358	3.730	1.490	0.990	109.830	276.000	34
0.359	4.080	1.250	0.940	31.000	260.000	35
0.337	8.010	8.670	0.230	48.730	303.000	36

0.369	4.810	1.200	0.920	101.500	319.000	37
0.359	4.665	2.324	1.030	280.700	296.000	38
0.395	4.996	2.025	1.080	2264.000	305.000	39
0.386	3.491	1.707	1.050	630.000	310.000	40
0.356	6.983	3.617	1.010	228.560	250.000	41
0.358	2.950	1.140	0.880	104.000	195.500	42
0.349	3.150	2.160	1.120	54.000	125.000	43
0.351	3.900	1.930	1.000	48.000	93.000	43
0.375	17.456	1.624	1.090	87.900	297.000	44
0.368	4.140	0.940	0.940	171.000	279.000	45
0.379	4.110	1.030	0.920	531.670	247.800	46
0.366	2.820	1.170	1.130	306.400	269.000	47
0.370	17.456	2.166	0.950	68.780	265.000	48
0.356	6.983	1.713	1.020	163.300	212.700	49
0.361	3.480	1.070	1.010	316.200	253.900	50
0.361	5.810	1.550	1.080	9.500	162.000	51
0.368	4.010	0.930	0.980	168.000	144.400	52
0.378	7.745	1.803	1.120	228.000	252.000	53
0.346	3.410	1.260	1.050	99.000	238.000	54
0.372	11.654	1.476	0.894	458.000	151.800	55
0.368	3.280	1.040	0.990	75.800	186.000	56
0.387	4.200	0.940	0.990	1411.000	317.000	57
0.369	3.750	1.100	1.070	48.300	181.200	58

Table S4. Structural parameters of carbon for ICE.

d_{002} (nm)	L_a (nm)	L_c (nm)	I_D/I_G	SSA_{BET} (m^2 g^{-1})	ICE (%)	Reference
0.348	3.930	1.880	1.030	28.500	44.600	7
0.371	3.700	1.230	1.170	47.200	41.400	8
0.344	5.840	3.700	1.010	52.200	61.200	8
0.336	3.690	1.210	1.050	87.500	33.350	9
0.355	3.840	1.000	0.970	254.500	31.060	9
0.335	43.871	40.816	0.340	33.400	81.560	11
0.334	145.231	74.216	0.430	6.170	78.600	12
0.330	5.799	1.602	1.180	105.000	73.000	13
0.340	5.310	2.970	0.890	68.300	35.300	14
0.339	7.738	1.554	1.060	430.000	15.700	15
0.337	5.402	23.314	1.830	1551.800	50.100	16
0.425	8.728	2.308	1.020	1857.000	19.700	19
0.391	3.130	1.020	0.890	1030.500	25.000	20
0.353	17.599	1.551	1.670	995.000	23.800	21
0.356	43.641	4.069	1.060	69.200	19.000	22
0.371	3.490	1.060	0.970	1021.100	27.600	28
0.388	3.960	0.970	1.060	983.200	61.170	29
0.386	7.737	1.707	0.920	1950.000	32.000	30
0.379	3.980	0.940	0.950	778.750	24.400	31
0.353	3.370	0.770	0.810	110.730	19.800	33
0.358	3.730	1.490	0.990	109.830	35.300	34
0.359	4.080	1.250	0.940	31.000	24.100	35
0.369	4.810	1.200	0.920	101.500	47.000	37
0.359	4.665	2.324	1.030	280.700	20.000	38
0.395	4.996	2.025	1.080	2264.000	31.100	39
0.386	3.491	1.707	1.050	630.000	71.000	40
0.356	6.983	3.617	1.010	228.560	55.350	41
0.364	4.090	1.060	0.740	234.000	39.700	42
0.358	2.950	1.140	0.880	104.000	38.200	42
0.349	3.150	2.160	1.120	54.000	55.500	43
0.341	5.310	2.970	0.690	117.400	34.800	43
0.360	4.000	1.880	1.130	72.000	52.000	43
0.351	3.900	1.930	1.000	48.000	27.000	43
0.375	17.456	1.624	1.090	87.900	40.000	44

0.368	4.140	0.940	0.940	171.000	72.100	45
0.379	4.110	1.030	0.920	531.670	42.600	46
0.366	2.820	1.170	1.130	306.400	42.800	47
0.370	17.456	2.166	0.950	68.780	37.920	48
0.356	6.983	1.713	1.020	163.300	33.000	49
0.361	3.480	1.070	1.010	316.200	30.280	50
0.361	5.810	1.550	1.080	9.500	54.000	51
0.375	4.440	1.250	1.020	15.100	57.000	51
0.384	3.260	1.010	0.990	41.600	50.000	51
0.377	3.950	1.190	1.010	18.300	58.000	51
0.346	3.410	1.260	1.050	99.000	49.000	54
0.372	11.654	1.476	0.894	458.000	30.000	55
0.368	3.280	1.040	0.990	75.800	45.800	56
0.369	3.750	1.100	1.070	48.300	47.100	58
0.387	3.110	1.200	1.030	24.500	46.800	58
0.348	4.390	1.330	1.110	270.000	31.700	59
0.356	6.959	1.627	0.980	820.000	59.500	60
0.409	3.130	1.140	1.090	1089.000	63.600	61
0.347	3.480	0.930	0.910	416.350	48.400	62
0.376	3.780	1.100	0.950	99.600	49.100	63
0.378	3.230	0.970	0.790	176.900	55.100	63
0.351	2.610	1.350	0.770	20.330	43.200	64
0.381	4.280	0.870	0.990	519.000	29.400	64
0.386	5.819	1.544	0.820	377.600	41.800	65
0.419	2.590	0.650	0.740	88.450	50.700	66
0.411	2.850	0.980	0.870	356.980	40.800	66
0.378	3.930	0.750	1.040	668.800	24.600	67
0.378	4.510	1.020	0.860	5.000	31.500	68
0.380	2.660	0.990	0.910	3.400	58.300	69
0.395	11.658	1.473	1.090	398.850	50.400	70
0.384	4.850	1.150	1.260	336.400	50.690	71
0.403	3.620	1.220	1.160	65.000	61.800	72
0.383	4.190	1.070	1.010	354.700	73.000	73
0.378	4.150	1.060	1.070	132.000	72.000	73
0.398	3.950	1.140	0.900	19.100	45.700	74

0.349	**3.700**	**1.260**	**1.000**	**534.200**	**37.700**	**75**
0.342	**15.869**	**2.174**	**1.080**	**757.800**	**44.200**	**76**

Table S5. Prediction of capacity structural parameters.

d_{002} (nm)	L_a (nm)	L_c (nm)	I_D/I_G	SSA_{BET} (m^2 g^{-1})	Measured Capacity (mAh g^{-1})	Predicted Capacity (mAh g^{-1})	MAE
0.340	5.202	3.942	0.676	371.535	240.000	255.199	8.830
0.350	4.393	1.298	0.958	331.577	362.000	356.652	
0.400	4.813	0.774	1.067	224.995	602.000	607.944	

Table S6. Prediction of ICE structural parameters.

d_{002} (nm)	L_a (nm)	L_c (nm)	I_D/I_G	SSA_{BET} (m^2 g^{-1})	Measured ICE (%)	Predicted ICE (%)	MAE
0.340	5.202	3.942	0.676	371.535	57.000	53.486	2.390
0.350	4.393	1.298	0.958	331.577	27.250	30.315	
0.400	4.813	0.774	1.067	224.995	57.990	57.398	

Reference

[1] G. Kresse, J. Hafner, *Phys. Rev. B* 1994, **49**, 14251.

[2] D. Toghraie, N. Sina, M. Mozafarifard, A. a. Alizadeh, F. Soltani, M. A. Fazilati, *Heat. Transf. Res.* 2020, **51**, 1351.

[3] R. Ding, R. Wang, Y. Ding, W. Yin, Y. Liu, J. Li, J. Liu, *Angew. Chem. Int. Ed.* 2020, **59**, 19175.

[4] F. Y. Dalkiran, M. Toraman, *Aircr. Eng. Aerosp. Tec.* 2021, **93**, 35.

[5] M. Achite, F. B. Banadkooki, M. Ehteram, A. Bouharira, A. N. Ahmed, A. Elshafie, *Stoch. Env. Res. Risk. A.* 2022, **36**, 1835.

[6] P. Xiong, X. Zhao, Y. Xu, *ChemSusChem,* 2018, **11**, 202.

[7] Q. Sun, D. Li, J. Cheng, L. Dai, J. Guo, Z. Liang, L. Ci, *Carbon,* 2019, **155**, 601.

[8] Y. Qian, S. Jiang, Y. Li, Z. Yi, J. Zhou, J. Tian, N. Lin, Y. Qian, *Angew. Chem. Int. Ed.* 2019, **58**, 18108.

[9] Y. Zhang, L. Li, W. Hong, T. Qiu, L. Xu, G. Zou, H. Hou, X. Ji, S. Li, *Mater. Chem. Phys.* 2019, **236**, 121809.

[10] Y. Liu, Y.-X. Lu, Y.-S. Xu, Q.-S. Meng, J.-C. Gao, Y.-G. Sun, Y.-S. Hu, B.-B. Chang, C.-T. Liu, A.-M. Cao, *Adv. Mater.* 2020, **32**, 2000505.

[11] Y. An, H. Fei, G. Zeng, L. Ci, B. Xi, S. Xiong, J. Feng, *J. Power Sources,* 2018, **378**, 66.

[12] Z. Tai, Q. Zhang, Y. Liu, H. Liu, S. Dou, *Carbon,* 2017, **123**, 54.

[13] J. Ge, B. Wang, J. Zhou, S. Liang, A. M. Rao, B. Lu, *ACS Mater. Lett.* 2020, **2**, 853.

[14] J. Hu, Y. Xie, M. Yin, Z. Zhang, *J. Energy Chem.* 2020, **49**, 327.

[15] D. Li, X. Cheng, R. Xu, Y. Wu, X. Zhou, C. Ma, Y. Yu, *J. Mater. Chem. A,* 2019, **7**, 19929.

[16] J. Chen, J. Feng, L. Dong, C. Long, D. Li, *J. Electroanal. Chem.* 2020, **862**, 113902.

[17] H. Luo, M. Chen, J. Cao, M. Zhang, S. Tan, L. Wang, J. Zhong, H. Deng, J. Zhu, B. Lu, *Nano-Micro Lett.* 2020, **12**, 113.

[18] Y. Feng, S. Chen, J. Wang, B. Lu, *J. Energy Chem.* 2020, **43**, 129.

[19] Y. Liu, B. Huang, L. Zheng, M. Shen, Z. Pu, Y. Shao, X. Li, S. Liao, *RSC Adv.* 2021, **11**, 1039.

[20] J. Yang, Z. Ju, Y. Jiang, Z. Xing, B. Xi, J. Feng, S. Xiong, *Adv. Mater.* 2018, **30**, 1700104.

[21] W. Wei, Y. Zheng, M. Huang, J. Shi, L. Li, Z. Shi, S. Liu, H. Wang, *Nanoscale,* 2021, **13**, 4911.

[22] S. Chen, Y. Feng, J. Wang, E. Zhang, X. Yu, B. Lu, *Sci. China Mater.* 2021, **64**, 547.

[23] Y. Zhang, L. Li, Y. Xiang, G. Zou, H. Hou, W. Deng, X. Ji, *ACS Appl. Mater. Interfaces,* 2020, **12**, 30431.

[24] X. Wang, J. Zhao, D. Yao, Y. Xu, P. Xu, Y. Chen, Y. Chen, K. Zhu, K. Cheng, K. Ye, J. Yan, D. Cao, G. Wang, *J. Electroanal. Chem.* 2020, **871**, 114272.

[25] W. Zhang, Z. Cao, W. Wang, E. Alhajji, A.-H. Emwas, P. M. F. J. Costa, L. Cavallo, H. N. Alshareef, *Angew. Chem. Int. Ed.* 2020, **59**, 4448.

[26] L. Liu, Y. Chen, Y. Xie, P. Tao, Q. Li, C. Yan, *Adv. Funct. Mater.* 2018, **28**, 1801989.

[27] Y. Zuo, P. Li, R. Zang, S. Wang, Z. Man, P. Li, S. Wang, W. Zhou, *ACS Appl. Energy Mater.* 2021, **4**, 2282.

[28] W. Xiong, J. Zhang, Y. Xiao, Y. Zhu, Z. Wang, Z. Lu, *Chem. Commun.* 2020, **56**, 3433.

[29] M. Chen, W. Wang, X. Liang, S. Gong, J. Liu, Q. Wang, S. Guo, H. Yang, *Adv. Energy Mater.* 2018, **8**, 1800171.

[30] S. Kim, M. Ju, J. Lee, J. Hwang, J. Lee, *J. Am. Chem. Soc.* 2020, **142**, 9250.

[31] H. Li, Z. Cheng, Q. Zhang, A. Natan, Y. Yang, D. Cao, H. Zhu, *Nano Lett.* 2018, **18**, 7407.

[32] D. M. Zhang, Z. W. Chen, J. Bai, C. C. Yang, Q. Jiang, *Batteries Supercaps,* 2020, **3**, 185.

[33] L. Wang, S. Li, J. Li, S. Yan, X. Zhang, D. Wei, Z. Xing, Q. Zhuang, Z. Ju, *Mater. Today Energy* 2019, **13**, 195.

[34] Y. Liu, H. Dai, L. Wu, W. Zhou, L. He, W. Wang, W. Yan, Q. Huang, L. Fu, Y. Wu, *Adv. Energy Mater.* 2019, **9**, 1901379.

[35] X. Zhao, P. Xiong, J. Meng, Y. Liang, J. Wang, Y. Xu, *J. Mater. Chem. A,* 2017, **5**, 19237.

[36] Z. Liu, J. Wang, X. Jia, W. Lo, Q. Zhang, L. Fan, H. Ding, H. Yang, X. Yu, X. Li, B. Lu, *ACS Nano,* 2019, **13**, 10631.

[37] J. Ruan, Y. Zhao, S. Luo, T. Yuan, J. Yang, D. Sun, S. Zheng, *Energy. Storage. Mater.* 2019, **23**, 46.

[38] P. Li, J.-Y. Hwang, S.-M. Park, Y.-K. Sun, *J. Mater. Chem. A,* 2018, **6**, 12551.

[39] Z. Sang, D. Su, J. Wang, Y. Liu, H. Ji, *Chem. Eng. J.* 2020, **381**, 122677.

[40] X. Li, N. Sun, X. Tian, T. Yang, Y. Song, B. Xu, Z. Liu, *Energy Fuels,* 2020, **34**, 2445.

[41] X. Lu, X. Pan, Z. Fang, D. Zhang, S. Xu, L. Wang, Q. Liu, G. Shao, D. Fu, J. Teng, W. Yang, *ACS Appl. Mater. Interfaces,* 2021, **13**, 41619.

[42] M. Yang, J. Dai, M. He, T. Duan, W. Yao, *J. Colloid Interface Sci.* 2020, **567**, 256.

[43] X. Wang, K. Han, D. Qin, Q. Li, C. Wang, C. Niu, L. Mai, *Nanoscale,* 2017, **9**, 18216.

[44] W. Li, D. Wang, Z. Gong, X. Guo, J. Liu, Z. Zhang, G. Li, *Carbon,* 2020, **161**, 97.

[45] D.-S. Bin, X.-J. Lin, Y.-G. Sun, Y.-S. Xu, K. Zhang, A.-M. Cao, L.-J. Wan, *J. Am. Chem. Soc.* 2018, **140**, 7127.

[46] W. Cao, E. Zhang, J. Wang, Z. Liu, J. Ge, X. Yu, H. Yang, B. Lu, *Electrochim. Acta,* 2019, **293**, 364.

[47] H. He, D. Huang, Y. Tang, Q. Wang, X. Ji, H. Wang, Z. Guo, *Nano Energy,* 2019, **57**, 728.

[48] W. Hong, Y. Zhang, L. Yang, Y. Tian, P. Ge, J. Hu, W. Wei, G. Zou, H. Hou, X. Ji, *Nano Energy* 2019, **65**, 104038.

[49] Y. Sun, Y. Zhang, Z. Xing, D. Wei, Z. Ju, Q. Zhuang, *Sustainable Energy Fuels,* 2020, **4**, 1216.

[50] X. Qi, K. Huang, X. Wu, W. Zhao, H. Wang, Q. Zhuang, Z. Ju, *Carbon,* 2018, **131**, 79.

[51] C. Chen, M. Wu, Y. Wang, K. Zaghib, *J. Power Sources,* 2019, **444**, 227310.

[52] N. Sun, Q. Zhu, B. Anasori, P. Zhang, H. Liu, Y. Gogotsi, B. Xu, *Adv. Funct. Mater.* 2019, **29**, 1906282.

[53] J. Ruan, X. Wu, Y. Wang, S. Zheng, D. Sun, Y. Song, M. Chen, *J. Mater. Chem. A,* 2019, **7**, 19305.

[54] Y. Xu, C. Zhang, M. Zhou, Q. Fu, C. Zhao, M. Wu, Y. Lei, *Nat. Commun.* 2018, **9**, 1720.

[55] M. Liu, L. Chang, J. Wang, J. Li, J. Jiang, G. Pang, H. Wang, P. Nie, C. Zhao, T. Xu, L. Wang, *J. Power Sources,* 2020, **469**, 228415.

[56] Y. Zhang, L. Yang, Y. Tian, L. Li, J. Li, T. Qiu, G. Zou, H. Hou, X. Ji, *Mater. Chem. Phys.* 2019, **229**, 303.

[57] G. Xia, C. Wang, P. Jiang, J. Lu, J. Diao, Q. Chen, *J. Mater. Chem. A,* 2019, **7**, 12317.

[58] S. Alvin, C. Chandra, J. Kim, *Chem. Eng. J.* 2020, **391**, 123576.

[59] Z. Wu, L. Wang, J. Huang, J. Zou, S. Chen, H. Cheng, C. Jiang, P. Gao, X. Niu, *Electrochim. Acta* 2019, **306**, 446.

[60] X. Zhou, L. Chen, W. Zhang, J. Wang, Z. Liu, S. Zeng, R. Xu, Y. Wu, S. Ye, Y. Feng, X. Cheng, Z. Peng, X. Li, Y. Yu, *Nano Lett.* 2019, **19**, 4965.

[61] W. Wang, J. Zhou, Z. Wang, L. Zhao, P. Li, Y. Yang, C. Yang, H. Huang, S. Guo, *Adv. Energy Mater.* 2018, **8**, 1701648.

[62] H. Ma, X. Qi, D. Peng, Y. Chen, D. Wei, Z. Ju, Q. Zhuang, *Chemistryselect,* 2019, **4**, 11488.

[63] C. Gao, Q. Wang, S. Luo, Z. Wang, Y. Zhang, Y. Liu, A. Hao, R. Guo, *J. Power Sources,* 2019, ***415***, 165.

[64] N. Xiao, X. Zhang, C. Liu, Y. Wang, H. Li, J. Qiu, *Carbon,* 2019, **147**, 574.

[65] S. Chen, K. Tang, F. Song, Z. Liu, N. Zhang, S. Lan, X. Xie, Z. Wu, *Nanotechnology,* 2022, **33**, 055401.

[66] R. C. Cui, B. Xu, H. J. Dong, C. C. Yang, Q. Jiang, *Adv. Sci.* 2020, **7**, 1902547.

[67] L. Tao, L. Liu, R. Chang, H. He, P. Zhao, J. Liu, *J. Power Sources,* 2020, **463**, 228172.

[68] X. Wu, C. W. K. Lam, N. Wu, S.-S. Pang, Z. Xing, W. Zhang, Z. Ju, *Mater. Today Energy,* 2019, **11**, 182.

[69] Q. Wang, C. Gao, W. Zhang, S. Luo, M. Zhou, Y. Liu, R. Liu, Y. Zhang, Z. Wang, A. Hao, *Electrochim. Acta,* 2019, **324**, 134902.

[70] H. Zhang, C. Luo, H. He, H.-H. Wu, L. Zhang, Q. Zhang, H. Wang, M.-S. Wang, *Nanoscale Horiz.* 2020, **5**, 895.

[71] S. Tian, D. Guan, J. Lu, Y. Zhang, T. Liu, X. Zhao, C. Yang, J. Nan, *J. Power Sources,* 2020, **448**, 227572.

[72] Z. Jian, Z. Xing, C. Bommier, Z. Li, X. Ji, *Adv. Energy Mater.* 2016, **6**, 1501874.

[73] X. Journal of Power SourcesHe, J. Liao, Z. Tang, L. Xiao, X. Ding, Q. Hu, Z. Wen, C. Chen, *J. Power Sources,* 2018, **396**, 533.

[74] Y. Qian, S. Jiang, Y. Li, Z. Yi, J. Zhou, T. Li, Y. Han, Y. Wang, J. Tian, N. Lin, Y. Qian, *Adv. Energy Mater.* 2019, **9**, 1901676.

[75] Z. Qiu, K. Zhao, J. Liu, S. Xia, *Electrochim. Acta,* 2020, **340**, 135947.

[76] G. Wang, X. Xiong, D. Xie, Z. Lin, J. Zheng, F. Zheng, Y. Li, Y. Liu, C. Yang, M. Liu, *J. Mater. Chem. A,* 2018, **6**, 24317.